Influence of Multi-Pass Friction Stir Processing on the Corrosion Behavior of an Al-Mg-Si Alloy

Citation for the original published paper (version of record):
Esmaily, M., Mortazavi Seyedeh, N., Osikowicz, W. et al (2016). Influence of Multi-Pass Friction Stir Processing on the Corrosion Behavior of an Al-Mg-Si Alloy. Journal of the Electrochemical Society, 163(3): C124-C130. http://dx.doi.org/10.1149/2.1091603jes

(article starts on next page)

Journal of The Electrochemical Society

Influence of Multi-Pass Friction Stir Processing on the Corrosion Behavior of an Al-Mg-Si Alloy

Influence of Multi-Pass Friction Stir Processing on the Corrosion Behavior of an Al-Mg-Si Alloy

M. Esmaily,[a,*,z] N. Mortazavi,[b] W. Osikowicz,[c] H. Hindsefelt,[c] J. E. Svensson,[a,**] M. Halvarsson,[b] G. E. Thompson,[d,**] and L. G. Johansson[a]

[a]*Department of Chemical and Biological Engineering, Chalmers University of Technology, SE-412 96 Gothenburg, Sweden*
[b]*Department of Applied Physics, Chalmers University of Technology, SE-412 96 Gothenburg, Sweden*
[c]*Sapa Technology, SE-612 81 Finspang, Sweden*
[d]*School of Materials, The University of Manchester, Manchester M13 9PL, United Kingdom*

The effect of multi-pass (100% overlap) friction stir processing (FSP) on the NaCl-induced atmospheric corrosion behavior of an extruded 6005-T6 aluminum alloy has been studied. Samples were contaminated with 70 and 200 μg/cm^2 NaCl and exposed in the presence of 400 ppm CO_2 for a time interval of 200–3200 h. The results showed that increasing the number of passes gives rise to several crucial changes in the microstructure of the processed regions. Gravimetric analyses and morphological inspections of the corroded samples revealed that multi-pass FSP has also a significant impact on the NaCl-induced atmospheric corrosion behavior of the FS processed samples. While increasing the number of FSP passes resulted in a reduced extent of pitting corrosion in the stir zone, it induced a significant pitting corrosion attack in the heat affected zone of the samples, which were shown to be linked to a reduction in the size of intermetallic particles in the stir zone of the multi-pass FSP specimens. The results also showed that the cathodic activity of intermetallic particles in this family of Al alloys is size-dependent.
 [DOI: 10.1149/2.1091603jes]

Manuscript submitted October 2, 2015; revised manuscript received December 26, 2015. Published January 5, 2016.

Extruded Al-Mg-Si (AA 6xxx-series) aluminum alloys are employed in lightweight construction structures in, e.g., automotive, marine and architectural applications.[1] In all these application, welding is inevitable. Friction stir welding (FSW) is a sustainable welding technique for joining lightweight materials, especially Al alloys. During the last two decades, extensive investigations have been devoted to the microstructure and mechanical properties of FSW 6xxx series Al alloys.[2–10] The basic precipitation sequence for ternary Al-Mg-Si alloys is generally considered to be: SSSS (α-super saturated) → Clusters → Guinier–Preston (GP) zones → β″ → β′ → β, where β″ and β′ precipitates are usually needle- and rod-like. They are metastable precursors of the equilibrium β (Mg_2Si) phase which forms platelet-shaped particles in the alloys' microstructure.[11,12] Using high-resolution microscopy, Sato et al.[13] and others, see e.g., Refs. 14–16 report that during FSW of this family of Al alloys, the β″ precipitates are dissolved in the stir zone (SZ) while they remain in the thermo-mechanically affected zone (TMAZ). It is also reported that large Si- and Fe-rich phase particles in the SZ of FS welds become fragmented but do not dissolve.

Over the past two decades, friction stir processing (FSP), which is a variant of FSW, has established itself as a promising generic metallurgical tool for microstructural modifications in metallic materials.[17] FSP provides the opportunity to manipulate the microstructural properties in terms of mean grain size, precipitation state, texture and distribution of residual stresses across the processed area in various types of metallic materials, including Al alloys.[18–20] This solid-state process has been employed for fabrication of superplastic-fine-grained 7xxx series Al alloys (exhibiting elongations up to 200%) as well as Al alloys with high room temperature formability.[21–23] FSP has also been successfully used in powder metallurgy, i.e., producing metal matrix composites with a uniform distribution of reinforcements in the host matrix.[23] This unique metallurgical tool can also be employed for multi-pass processing in Al alloys. From a technological standpoint, full length multi-pass FS welding/processing is rather uncommon in normal welding practices. However, it is utilized as a repair procedure if the required weld quality is not reached with the first pass. More commonly, a partial multi-pass FS processing is applied, most notably in two dimensional welding. Such instances are indeed very common, especially in close path welding and whenever crossing of the welding paths is executed. Multi-pass FSP can also produce Al alloys with superplastic properties, which is shown by Johannes et al.,[24] who examined the usefulness of FSP in creating large areas of superplastic material in an AA7075 Al alloy.

The FSP studies mentioned above, mainly focus on 2xxx and 7xxx Al alloys. Thus, the work directed to elucidating the effect of multi-pass FSP on the properties of Al-Mg-Si alloys is relatively limited. Ma et al.[25,26] conducted five-pass FSP, with 50% overlap, on a Al-Si-Mg A356 cast alloy and reported that overlapping FSP does not exert a substantial effect on the size and distribution of the Si-containing particles. They also reported that the strength and ductility of the transitional zones between two FSP passes were slightly lower than those of the nugget zones. El-Rayes et al.[27] investigated the influence of multi-pass FSP, with 100% overlap, on the microstructural and mechanical properties of AA6082-T651 and reported that the grain size, dissolution of hardening β″ and fragmentation of second phase particles increased with increasing the number of FSP passes. Al-Fadhalah et al.[28] studied the effect of overlapping (25, 50 and 75%) between consecutive passes of FSP on the microstructure, microtexture, and mechanical properties of AA6063 Al alloy. They reported that increasing the percentage of overlapping induces limited change in the grain size in the overlapping area, but results in formation of an increased fraction of sub-grain boundaries in the TMAZ.

The corrosion properties of FSW 6xxx series Al alloys have been studied in a number of publications,[29–31] but to a much smaller extent compared to the work dedicated to the microstructural and mechanical properties of FSW joints made of this family of alloys. Working on the corrosion behavior of AA6061-T6 Al weldments produced by FSW and gas tungsten arc welding (GTAW) in an aqueous solution of NaCl, Fahimpour et al.[30] reported that the corrosion resistance of the FSW specimens was better than that of the GTAW. More recently, Gharavi et al.[31] investigated the aqueous corrosion behavior of the AA6061-T6 alloy fabricated by FSW in an aerated solution with a pH of 6.5 by means of electrochemical impedance spectroscopy and cyclic polarization experiments. They stated that FSW promotes the corrosion susceptibility of the alloy and that pitting corrosion associated with intergranular attack was the dominant corrosion type in the weld zones and the base material (BM).

Currently, there are no reported investigations of the effect of multi-pass FSP on the corrosion behavior of 6xxx series Al alloys. Also, the influence of FSW/P on the atmospheric corrosion

*Electrochemical Society Student Member.
**Electrochemical Society Active Member.
[z]E-mail: mohsen.esmaily@chalmers.se

Table I. Chemical composition (in weight percentage) of the alloy tested in this study.

Alloy	Mg	Si	Mn	Cu	Fe	Cr	Ti	Al
AA6005-T6	0.55	0.55	0.45	0.25	0.19	0.13	0.08	Bal.

behavior of Al alloys has not been subjected to scientific study. Hence, in the present study we analyzed the corrosion behavior of multi-pass FSP extruded AA6005-T6 Al alloy in a carefully controlled humid air environment, i.e., simulating a sheltered out-door environment. Quantitative analyses were performed on the pitting corrosion behavior of the main processing zones, e.g., SZ and HAZ. An attempt was made to relate the corrosion behavior of these regions to the microstructural changes introduced by multi-pass FSP. Special emphasis is put on the role of the intermetallic size/number density on the corrosion behavior of FSP specimen.

Experimental

The material used in this study was 10 mm thick extruded AA 6005-T6 profile. The chemical composition of the BM was analyzed using an optical mass spectroscope (Table I). The extruded material was cut to plates of 300 mm length and 250 mm width. Single-, double- and triple-pass FSPs with 100% overlap were conducted parallel to the extrusion direction (ED) at a constant rotational speed of 1200 rpm and a traverse speed of 500 mm/min. The time interval between each FSP pass was 5 minutes. As a result, the plates were pre-heated for the second and third passes. After completion of the processing, samples were cooled in ambient air. The tool consisted of a Triflat conical pin with a 10 mm diameter pin crown, a 8 mm diameter pin tip and a pin length of 9.8 mm. The tool featured a concave shoulder which was 24 mm in diameter. The tool was applied with a tilt angle of 2.0°.

The single-, double- and triple-pass FSP samples were cross-sectioned perpendicular to the process direction for microstructural examinations using electrical discharge cutting machine to prevent thermal degradation. A solution of 1.2 ml hydrofluoric acid (HF) + 1.8 ml hydrochloric acid (HCl) + 2 ml nitric acid (HNO_3) + 95 ml water was used to reveal the macro- and microstructural features. The soundness of the samples was initially examined by means of visual inspections. Additionally, the cross-sections were inspected using a Nikon SMZ-745T (SMZ745T) stereomicroscope and an Olympus GX-71 optical microscope (OM) for examining the presence of weld imperfections. A FEI Quanta 200 environmental scanning electron microscope (ESEM), equipped with Oxford Inca energy dispersive X-ray (EDX) micro-analysis hardware, was used for imaging. Analyzing the size of grains in the SZs of the processed samples and the BM was done using a LEO Ultra 55 field emission gun SEM equipped with an HKL Channel 5 electron backscatter diffraction (EBSD) system. The average grain size of the SZs were determined from 550–800 grains (processed by the EBSD). The sectioned samples were first ground on 500, 1200 and 4000 emery papers and polished using 3 and 0.25 μm diamond pastes on a Buehler Microcloth with an inorganic lubricant. Thereafter, they were electrochemically polished at −12°C using an electrolyte of methanol (CH_3OH) + 70% perchloric acid ($HClO_4$) (80:20) at 11 V dc. In addition, image processing and analyses were performed using ImageJ and Image Pro-Plus software in order to determine the size and number density of second phase particles.

Atmospheric corrosion exposures were conducted at ambient temperature (22.00 ± 0.3°C) for a time interval of 200–3200 h. The experimental set-up for the corrosion exposures is described elsewhere.[32–34] Relative humidity (RH) was regulated to be 95 ± 0.3%. CO_2 was added from a cylinder to give a constant concentration of 400 ± 20 ppm, which was approximately the same level of CO_2 as in the out-door environment.[32,33] The corrosion coupons included the main process zone, i.e., HAZs (in the advancing side (AS) and retreating side (RS)) and SZ, with overall dimensions of 25 × 10 × 3 mm^3. The coupons were mechanically ground and polished according the abovementioned recipe. The samples were contaminated with 70 and 200 μg/cm^2 NaCl. These values equates to 550 and 1570 μg/cm^{2}y of chloride ions respectively, which correspond to the concentrations of chloride ions in urban areas and marine environments, but not in the immediate vicinity of the coastline.[34] Deposition of salt was performed by spraying a solution of distilled water, ethanol and NaCl on the samples; see[34,35] for more details. The metal loss values were determined by removing the corrosion products using the leaching and pickling. To perform this, water-soluble corrosion products and remaining NaCl were first leached by immersing the corroded samples in ultrapure water for several periods of 1, 2, 30 and 45 min at 25°C. Afterwards, the samples were pickled in a solution of 50 ml H_3PO_4 (85%) and 20 g CrO_3/dm^3 in 1000 ml water at 80°C for 5 min. The corrosion product removal procedure on heavily corroded samples was carried out up to 45 times. Self-corrosion during the corrosion removal procedures was insignificant. The number density and depths of corrosion pits formed on the SZ and HAZ of the each sample were examined by utilising an interference microscope (RST plus) from WYKO†. The microscope was set to vertical scanning-interferometry mode with a focus area of 2 × 2 mm^2. The interference microscope employed in this study was a white light scanning instrument with a measurement range of 0.5 mm and a resolution of about 10 nm.

Results and Discussion

Macro- and microstructure of the processed samples.—Visual inspections of the FSP samples revealed the absence of volumetric defects on the surfaces. Only small amounts of flash formation were evident on the top of the processed samples. Figure 1 reveals transverse cross-sectional overviews of the three FSP samples. The

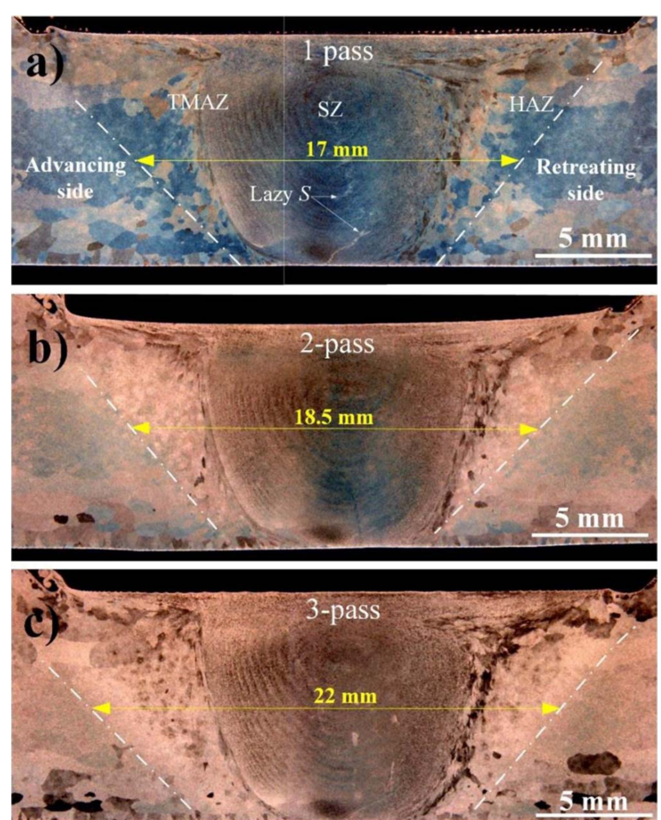

Figure 1. Pictures taken by stereomicroscope showing the cross-section of the FSP samples: (a) single-pass FSP; (b) double-pass FSP; and (c) triple-pass FSP. Attention is drawn to the difference in the width of the affected zone in the samples, shown by arrows in the mid-thicknesses.

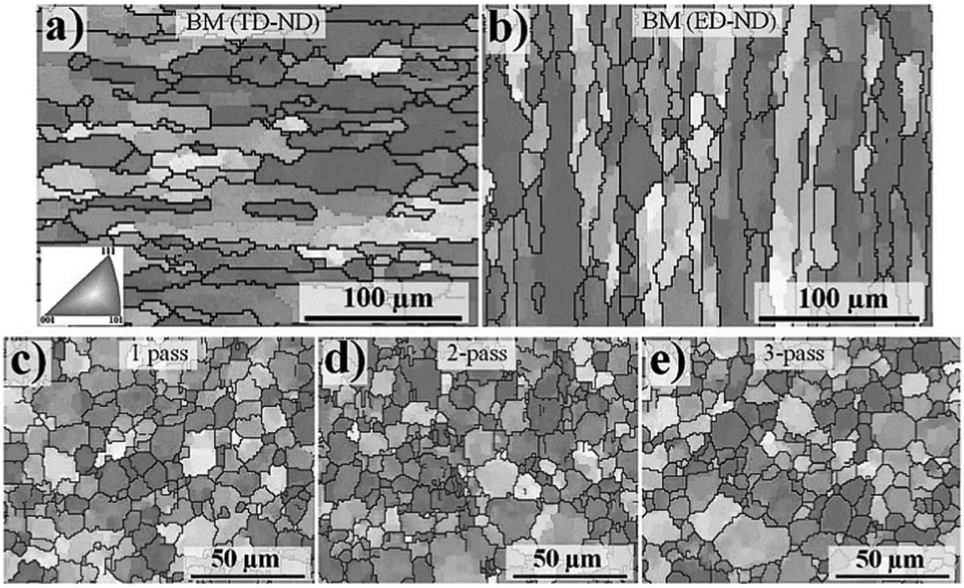

Figure 2. EBSD band contrast maps of (a) BM in TD-ND direction, (b) BM in ED-ND direction, (c) SZ of the single-, (d) double-, and (e) triple-pass FSP specimens.

cross-sections showed fully consolidated processed areas without imperfections, such as cavities, lack of penetration, or root defects. However, the presence of oxide particles appearing as semi-continuous bands, also known as kissing bonds or lazy *S*,[36] from the bottom to the top of the SZs was evident in the FSP samples. This imperfection is characterized as regions containing entrapped oxide particles originating from the faying surfaces of the workpieces causing the formation of less effective metallic bonds. This type of imperfection is usually formed in the SZ of Al alloy weldments produced by the FSW technique; see e.g., Refs. 36, 37. As expected, the cross-sections were quite similar in appearance. The main regions, i.e., SZ, TMAZ and HAZ, were recognizable in the cross-sections of all the samples. The characteristics of the TMAZ have been widely studied and it is usually regarded as a region of highly deformed structure, see e.g., Ref. 17.

In all the samples, fairly symmetrical TMAZ could be observed around the SZ on the AS and RS. However, while the transition between SZ and HAZ in the AS was sharp and clear, it was more diffused in the RS in all the processed specimens, which is a known characteristic of the TMAZ in FSW/Ped Al alloys.[14,17] The width of the TMAZ was estimated to be ∼1 mm. From the stereo-micrographs (Fig. 1), it was obvious that the width of the mid-thickness line in the affected zone, containing HAZs, TMAZs and the SZ, increased in the order single-pass < double-pass < triple-pass with values of ∼17, 18.5 and 22 mm, respectively. These values were cross checked using micro-hardness measurements (with a 100 gf load and 15 seconds dwell time) (not shown). The increase in the width of the HAZ due to consecutive passes was expected and is ascribed to both cumulative exposure to elevated temperatures and the pre-heating of the samples by each FS pass.

Figure 2 shows EBSD orientation maps (ED: extruded direction, ND: normal direction and TD: transverse directions) of the BM and SZs of the FSP samples. It may be noted that the EBSD maps in Figs. 3c–3e were acquired from the TD-ND direction of the

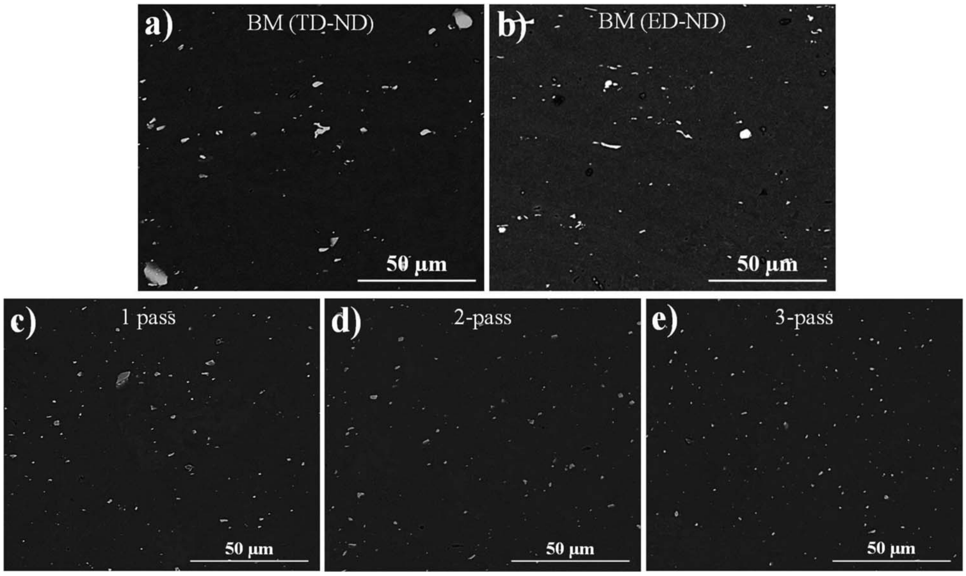

Figure 3. Scanning electron micrographs showing the distribution of second phase particles in (a) the BM in TD-ND direction, (b) the BM in ED-ND direction and (c) the SZ of the single-, (d) double- and (e) triple-pass FSP specimens.

processed extruded Al plates, i.e., the transverse cross-section of the FSP samples. As mentioned in the Experimental section, the aim of EBSD mapping was to document the grain sizes. Analyzing the texture, however, is beyond the scope of this paper and, hence, only EBSD 'band contrast' images are shown in Fig. 2. Inverse pole figure (IPF) maps revealed the typical fibrous grain structure of extruded Al alloys (BM). The average grain sizes of the regions shown in Figs. 2a and 2b were determined to be $\sim 128 \pm 28$ and 204 ± 12 μm, respectively. It is well-known[5,14,17] that the requirements for dynamic recrystallization, i.e., the minimum degree of plastic deformation and strain rate, are met during FSW/P of Al alloys. Thus, a fully recrystallized and equiaxed grain structure is usually developed in the SZ; as also demonstrated in Figs. 2c–2e. EBSD showed that the grain size increased slightly with increasing the number of passes. The average grain size in the SZ of the single- (Fig. 2c), double- (Fig. 2d) and triple-pass (Fig. 2e) FSP samples was determined to be ~22.7 (±5), 23.2 (±3) and 24.7 (±7) μm, respectively. The increase in size of α-Al grains with increasing number of FSP passes is in line with other studies, see, e.g., Refs. 27, 28. El-Rayes et al.,[27] who reported the same trend in the average size of grains by increasing the number of passes, attributed this to the grain coarsening arising from the additional/accumulated thermal cycles that the plate has experienced and the simultaneous occurrence of continuous dynamic recrystallization (CDRX) with each FSP pass. EBSD also revealed some useful information regarding the grain boundaries in the SZ of the FSP specimens. For all the FSP passes, the average fraction of high angle grain boundaries (HAGBs) was >72%, reaching its maximum value (~82%) in the SZ of the triple-pass FSP sample. Note that some properties of the Al alloys, such as fracture and intergranular corrosion (IGC), have been found to be strongly dependent on the nature of the grain boundaries and that a high fraction of HAGBs is reported to promote the IGC attack in Al alloys.[38–42]

Figure 3 shows SEM micrographs indicating the size and distribution of second phase particles in the same regions as the ones mapped by the EBSD in Fig. 2. 6xxx Al alloys exhibit complex sequences of precipitates. In addition to the sequence mentioned earlier, it is also known that the clustering and precipitation sequence can be altered by changing the Mg:Si ratio and/or adding additional alloying elements like Cu. Thus, in Cu-containing 6xxx Al alloys, the precipitation sequence is reported to be changed according to the following order; SSSS → Clusters → GP zones → β'' → β' → Q' → Q (lath-shaped) → Q + Si, where Q' is the precursor of the equilibrium Cu-rich Q phase.[11] The Cu-rich phases, which are partially responsible for intergranular corrosion, are usually observed in this family of Al alloys, especially in those containing high concentrations of Cu.[43] The formation of the sub-micron-sized particles in the different regions of FSW/Ped Al alloys is well-documented in the literature; see e.g., Ref. 43, and thus, will ne be treated here.

SEM/EDX showed that a range of Fe- intermetallic phases (Al-Fe, Al-Fe-Si and Al-Fe-Mn-Si), which are the typical particles for 6xxx Al alloys,[44] were present in the BM microstructure. In addition these, the intermetallic particles, seen in Figs. 3a–3e, were also Mg/Si-rich, similar to the chemical compositions of particles reported in Refs. 45, 46. The BM had larger second phase particles, ranging from 1–10 μm, than those in the SZ of all the processed samples. Further, it was qualitatively obvious that the size of particles in the SZs decreased with increasing the number passes from 1 to 3. Moreover, the number density of the particles increased with increasing the number of passes.

Figure 4 shows quantitative data related to the size and number density of second phase particles in the microstructure of the BM (TD-ND direction), the SZ and the HAZ of the FSP samples. It should be noted that only particles larger than 0.2 (±0.05) μm were quantified by image processing. The average size of second phase particles in the BM was ~3.8 (±0.2) μm. The average diameter of the particles in the HAZs increased only slightly with consecutive passes as compared to those in the BM. This is in accordance with previous reports on particle coarsening in the HAZs.[13] Considering the fact that FSP is a promising tool for fragmenting the particles in Al alloys,[27] the SZs showed a completely different number density and average diameter from those

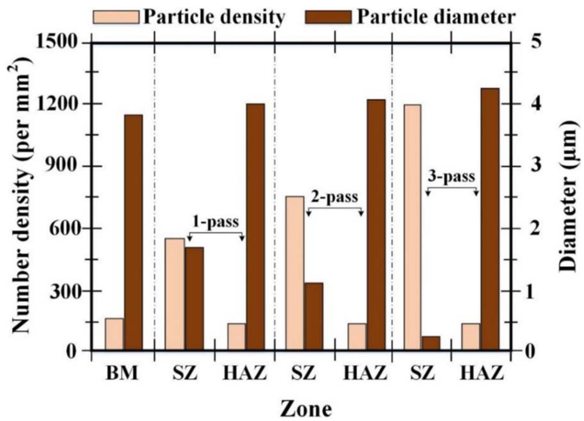

Figure 4. Quantitative data on the average diameter and number of second phase particles in the BM as well as SZ and HAZ of the FSP samples. The data presented were acquired from an area of 2 × 2 mm^2.

quantified in the microstructure of HAZs and the BM. In general, while the number density of particles in the SZs increased considerably as compared to those in the BM and HAZ, their average diameter decreased. Increasing the number of FSP passes further decreased the average diameter and increased the number density of second phase particles in the SZ. As an example, the number density of particles in the SZ increased by a factor of about 2 and the average diameter of the particles decreased by factor of about 6 when the number of FSP passes increased from 1 to 3. Thus, the results clearly showed that, in contrast to the grain size in the SZ, which was the finest in the single-pass FSP (compare Figs. 3c and 3e), intermetallics were much finer and appeared with a significantly higher number density in the SZ of triple-pass FSP sample.

Analyzing the corrosion behavior of the FSP samples.—*In the first set of exposures*, we deposited 70 μg/cm^2 NaCl on the surface of the specimens and exposed them for 1600 hours at ambient temperature and 95% RH. Figure 5 shows typical morphologies of the corroded surfaces of the SZ and HAZ of single-pass and triple-pass FSP samples. SEM analysis showed that while pitting corrosion and IGC were the dominant corrosion types in the SZs, the HAZ mainly

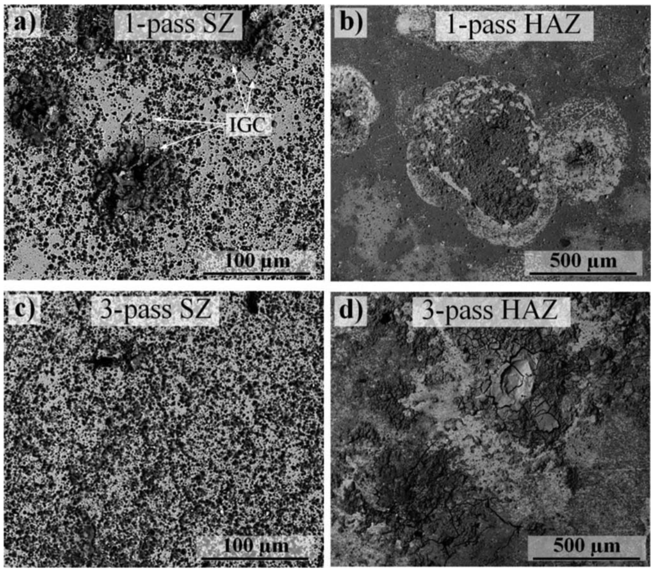

Figure 5. Scanning electron micrographs showing the morphologies of single- and triple-pass FSP corroded samples after 1600 h exposure in the presence of 70 μg/cm^2 NaCl and 400 ppm CO_2 at 95% RH.

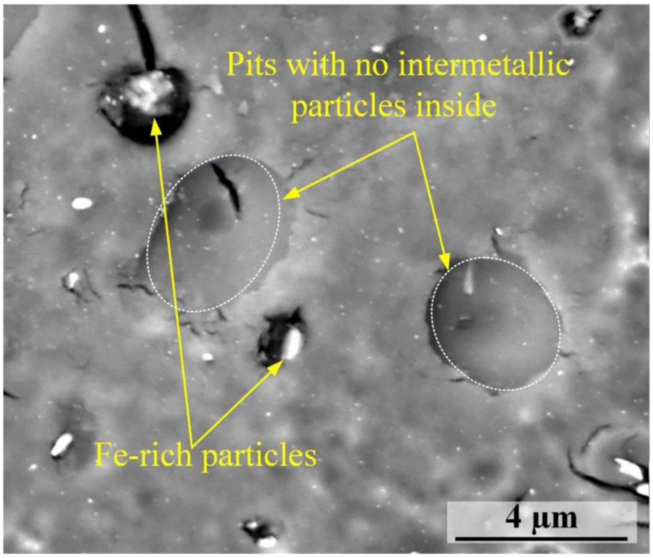

Figure 6. High-magnification SEM image showing the SZ of the triple-pass FSP sample after the corrosion product removal process. Note: Fe-rich particles were detected by SEM/EDX.

suffered pitting corrosion with very little evidence of IGC. It may be noted that some cracks and crack rings were observed, mainly on the corrosion products formed on the HAZs (Fig. 5d). This is likely related to shrinkage during drying after corrosion. While there was no evidence of large corrosion pits (>20 μm in diameter) in the SZ of the triple-pass FSP sample, they could be frequently detected is the SZ of the single-pass FSP specimen, as shown in Figs. 5a and 5b. Generally, the HAZ was more corroded than the SZ and the HAZ was less corroded in the single-pass FSP samples than in the triple-pass samples (Figs. 5b and 5d).

Figure 6 shows a high magnification SEM image taken from the SZ of the triple-pass FSP samples after 1600 h exposure. SEM/EDX on high-magnification SEM images showed that the tiny white particles are dispersoids consisting of α-Al(MnCrFe)Si phase precipitates. Dispersoids are small-sized, intermetallic particles (characteristically 0.05–0.4 μm) that are formed from elements such as Cr and Mn that exhibit a relatively low solubility in Al. Corrosion pits were not detected around the dispersoids. In Fig. 6, there were also two larger intermetallic particles (0.5–1.5 μm), designated as Fe-rich particles (by EDX), where corrosion pits were also present. In some cases, there was no evidence for intermetallic particles inside pits formed in the SZ (Fig. 6). It is suggested that this type of pitting corrosion occurred because of *either* the dissolution of an anodic precipitate *or* detachment of a cathodic particle due the corrosion product removal procedure.

In the second set of exposures, a considerably higher amount of NaCl (200 μg/cm^2) was sprayed to the surface of the samples to further accelerate corrosion. SEM analysis (Fig. 7) of the corroded surface of these samples revealed the same trend as for the samples exposed in the presence of 70 μg/cm^2 (Fig. 5). However, the more severe corrosion was occurred, which is indicative of the corrosive effect of NaCl toward Al and Al alloys, see the review paper of Frankel[47] for more details regarding the effect of Cl on pitting corrosion of Al alloys. Similar to the morphology of the samples in Fig. 5, the SZs were less corroded than the HAZs. When comparing the corrosion behavior of the single- and triple-pass FSP specimens, while the SZ of the triple-pass FSP specimen corroded milder than the SZ of the single-pass FSP specimen (compare Figs. 7a and 7d), the HAZ of the triple-pass FSP samples experienced the severest corrosion attack observed in this research (e.g., compare Figs. 7c and 7f).

Here, statistical analyses of the size distribution of the intermetallics (Fig. 4) showed that the SZ microstructure contained larger intermetallics in the single-pass samples than in the triple-pass FSP samples. From Figs. 7a and 7d, it is evident that the corrosion product accumulations formed in the SZ are much larger on the single-pass than on the triple-pass FSP samples. This clearly confirms that the cathodic activity of the intermetallic particles is size-dependent.

It should be noted that although the influence of the chemical composition of intermetallics on their cathodic/anodic activity of intermetallic particles in Al alloys is well-known (see the elegant researches by Birbilis et al.[48–50]), very few studies have analyzed the effect of the size of the intermetallic particles on the corrosion behavior of Al alloys. In this regard the following two studies should be cited. Dorin et al.,[51] who studied effect of cooling rate on the microstructure and the corrosion properties of Al-Fe alloys, reported that rapid solidification enhanced corrosion behavior of the alloys. They suggested that the smaller size of Fe-containing intermetallics in the microstructure of the rapidly cooled specimens was one the reasons for their improved corrosion resistance. Park et al.[52] studied the effect

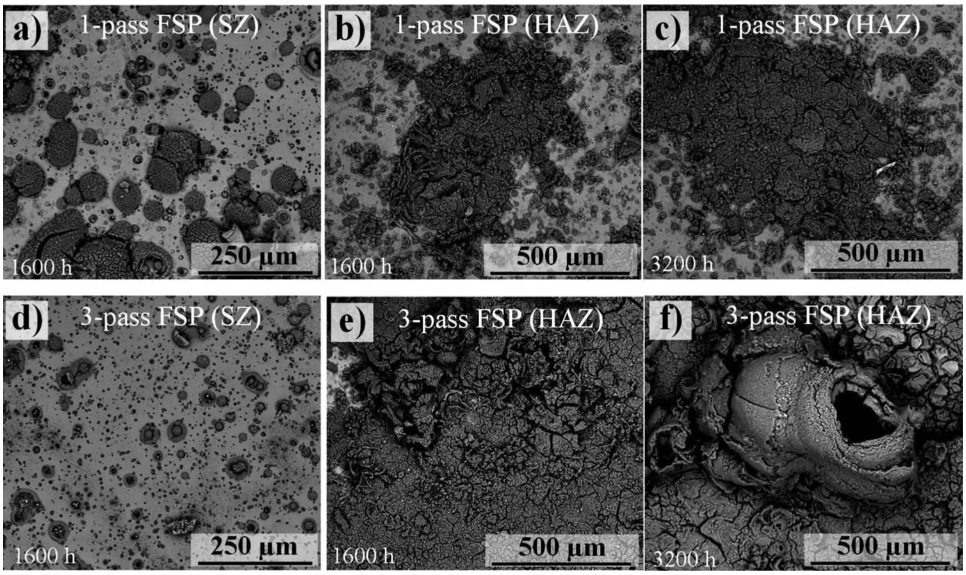

Figure 7. Scanning electron micrographs showing the morphologies of single- and triple-pass FSP corroded samples after 1600 and 3200 h exposure in the presence of 200 μg/cm^2 NaCl and 400 ppm CO_2 at 95% RH.

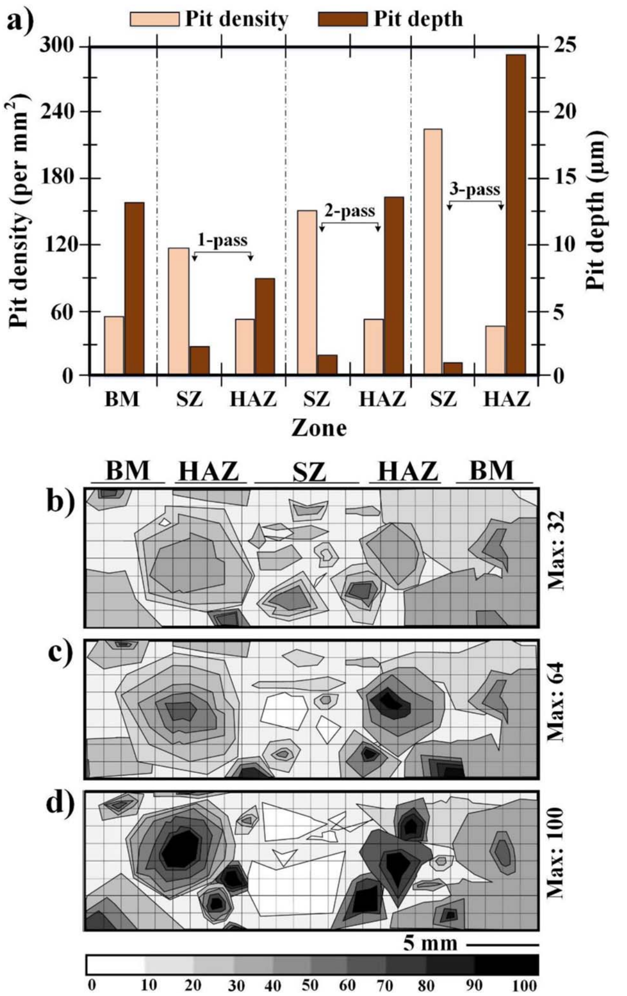

Figure 8. (a) Quantitative data on corrosion pits formed in the SZ and HAZ of the samples; (Exposure parameters: time: 200 h, NaCl amount: 70 μg/cm^2 NaCl, CO_2 concentration: 400 ppm, RH: 95% RH and T: 22°C). Contour plots showing the normalized pit depth distribution in; (b) single-, (c) double-, (d) triple-pass FSP samples.

of cathodically active intermetallic particles on pit initiation on AA 6061-T6. They reported that the extent of Al host matrix dissolution around intermetallic particles was, at first, independent of size. However, during later stages of corrosion particles did play a role, large pits forming around larger particles.

Figures 7a and 7d also show that, in many cases, circular features were detected in the SZs after the exposure. These features correspond to droplets consisting of NaCl (aq). Spherical corrosion products have also been observed on the surface of Mg alloys[33] upon exposure to atmospheric conditions in the presence of CO_2. It has been argued that the presence of ambient levels of CO_2 decreases the pH in the catholyte, resulting in a higher surface tension, which prevents spreading of the electrolyte.[34,35]

Quantitative analyses.—After corrosion product removal, the number density and depth of the corrosion pits were studied quantitatively (Fig. 8). In general and in line with the SEM investigations (Figs. 5 and 7), the SZs contained a much greater number of corrosion pits than the HAZs, however, the corrosion pits were considerably shallower in the SZs than in the HAZs.

Regarding the effect of multi-pass FSP on the microstructure of the SZs, it was evident that while an increasing number of passes increased the number of pits, the average pit depth decreased. The increase in the number density of pits from single- to triple-pass FSP is in accordance with the increase in the number density of intermetallic particles (Fig. 4). Regarding the HAZs, the number density of pits also coincides with the trend in the number density of intermetallic particles presented in Fig. 4. The depth of corrosion pits in the HAZ was increased noticeably with an increasing number of passes, which agrees well with the SEM micrographs; see e.g. Figs. 7c and 7f. Thus, while the average depth of the pits after 200 h exposure was ~6 μm in the HAZ of the single-pass FSP sample, the corresponding value for the triple-pass FSP sample was ~24 μm.

Figures 8b–8d shows contour plots summarizing the severity (depth) of pitting corrosion in different regions of single-, double- and triple-pass FSP samples. These contours were drawn from quantitative data obtained from optical profilometry. It was apparent that the SZ was less susceptible to pitting corrosion than the HAZ and BM. This was particularly the case for the triple-pass FSP sample (Fig. 8d). As displayed, the advancing side (AS) was more prone to corrosion attack than the retreating side (RS) of the weld. Several studies have reported that the AS experiences a higher peak temperature than the RS during FSW/P;[53,54] therefore a wider HAZ is expected to be developed on the AS (see Fig. 1) and this could explain the greater extent of atmospheric corrosion in the AS. Also, it may be noted that HAZs, especially in the AS, were much more corroded than the adjacent BM, which is in accordance with the results in Fig. 8a. The BM exhibited a somewhat non-homogenous distribution of pitting with the majority of damage close to the outer surfaces, the mid-thickness region being more resistant to pitting; see Figs. 8b–8d.

Figure 9 presents metal loss as a function of exposure time for all the processed material and the BM. Here, the samples (with dimensions of 25 × 10 × 3 mm^3 and containing all the processed zones) were exposed to 95% RH air with 400 ppm CO_2 at 22°C in the presence of 70 μg/cm^2 NaCl. As expected, the mass gain and metal loss data for the reference samples (exposed in the absence of NaCl) were in all cases negligible (<0.5 μm/year) and are not shown. The mass gain curve was initially linear in all cases and then becomes convex. The mass loss curves showed that the FSP materials exhibit totally different corrosion kinetics. Thus, the mass loss values of the single-pass FSP sample were much smaller than for the triple-pass FSP. Moreover, a close look into the data presented in Fig. 9 show that the mass gain curve for the triple-pass FSP sample became convex (or reach to the deceleration step) after much longer exposure time than the single-pass FSP sample (see the change in the slopes). It was also apparent that the BM exhibited smaller metal loss values than the least corroded FSP sample at all the exposure times.

To conclude, the results showed that the anodic and cathodic reactivities of the SZ and HAZ, respectively, were enhanced by the

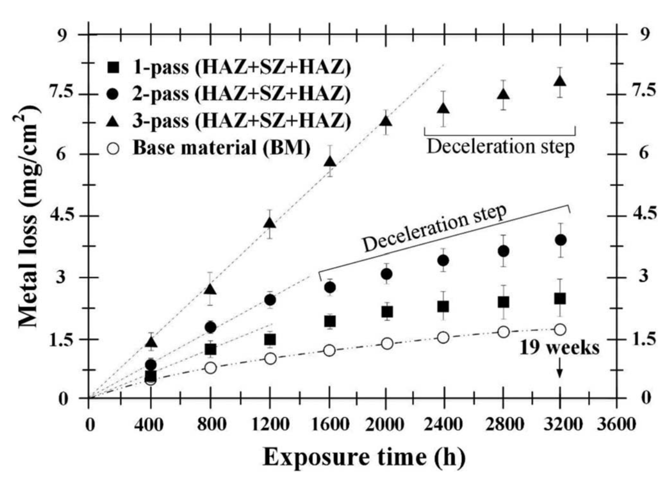

Figure 9. Metal loss data versus exposure time for the FSP samples and the BM. Triplicate samples were used for each condition to assess the reproducibility of the data. (Exposure parameters: NaCl amount: 200 μg/cm^2 NaCl, CO_2 concentration: 400 ppm, RH: 95% RH and T: 22°C).

increased number of FSP passes. The differences in the extent of corrosion in the HAZ of the single- and triple-pass FSP samples was clearly detectable in the SEM images (compare Figs. 7b and 7e as well as Figs. 7c and 7f). Thus, after 3200 h exposure the HAZ of the triple-pass FSP sample was much more corroded than that of the single-pass FSP samples.

As revealed by the EBSD presented here and other investigations cited in this study, multi-pass FSP has a minor effect on the size of grains in the microstructure of FS processed 6xxx Al alloys. Thus, the better corrosion resistance of the single-pass FSP sample in comparisons with the other two samples is likely linked to changes introduced to the characteristics of the intermetallic particles. The results presented here show that the size of the intermetallic particles plays an important role for the in the balance between anodic and cathodic activity of the different processed zones. Thus, the SZ of the triple-pass FSP sample, incorporating fragmented, and small-size intermetallic particles appears to act 'strongly' as a local cathode toward the HAZ and thus forms an active macro-galvanic corrosion cell. Such reactivity was, however, considered to be much less predominant in the single-pass FSP sample. In addition, bearing in mind that the metal losses are mainly related to the HAZ (e.g. Fig. 7), the increase in the rate of corrosion by increasing the number of FSP passes is partially related to the increase in the width of the HAZ (see the width of the affected zones in the mid-thickness of the samples in Fig. 1).

Conclusions

The results presented in this communication show that while multi-pass FSP has a minor impact on the size of α-Al grains in the SZ, it considerably decreases the average diameter of intermetallic particles in the SZ. It was also evident that the number of intermetallic particles in the SZ increases markedly with consecutive FSP passes. Such microstructural changes are shown to increase the overall rate of corrosion in the processed samples. This was attributed to the formation of strong macro-galvanic cells, where the SZ acts as a cathode and the surrounding HAZ is anode. Also, the increase in the width of the HAZ in multi-pass samples, which was the most vulnerable region to NaCl-induced atmospheric corrosion, contributes to the high corrosion rates observed in the multi-pass FSP samples. The results confirmed that the size of intermetallic particles in the SZ plays an important role in the cathodic activity of the SZ in FSW/Ped Al alloys. Consequently, the HAZ becomes more susceptible to atmospheric corrosion when the average size of intermetallic particles in the SZ is reduced. Moreover, it was confirmed that the cathodic activity of intermetallics depends on their size.

These results are of great technological importance since multi-pass FS processing/welding is frequently employed as a repair method and also being used in two dimensional joining in industries.

References

1. P. Marcus, *Corrosion Mechanisms in Theory and Practice*. CRC Press (2012).
2. M. Ericsson and R Sandström, *Int. J. Fatigue*, **25**, 1379 (2003).
3. K. Elangovan and V. Balasubramanian, *Mater. Des.*, **29**, 362 (2008).
4. S. R. Ren, Z.Y. Ma, and L. Q. Chen, *Scri. Mater.*, **56**, 69 (2007).
5. E. S. Takashi and Y. M. Song, *Int. J. Mater. Res.*, **105**, 883 (2014).
6. T. Morit and M. Yamanak, *Mater. Sci. Eng. A*, **595**, 196 (2014).
7. E. A. El-Danaf and M. M. El-Rayes, *Mater. Des.*, **46**, 561 (2013).
8. X. Sauvage, A. Dédé, A. Cabello Muñoz, and B. Huneau, *Mater. Sci. Eng. A*, **491**, 346 (2008).
9. U. Donatus, G. E. Thompson, X. Zhou, J. Wang, and K. Beamish, *Mater. Des.*, **83**, 203 (2015).
10. M. Cabibbo, H. J. McQueen, E. Evangelista, S. Spigarelli, M. Di Paola, and A. Falchero, *Mater. Sci. Eng. A*, **460–461**, 86 (2007).
11. U. Donatus, G. E. Thompson, X. Zhou, J. Wang, A. Cassell, and K. Beamish, *Mater. Charac.*, **107**, 85 (2015).
12. C. Ravi and C. Wolverton, *Acta Mater.*, **52**, 4213 (2004).
13. Y. Sato, H. Kokawa, M. Enomoto, and S. Jogan, *Metal. Mater. Trans. A*, **30**, 2429 (1999).
14. Y. Sato, H. Kokawa, M. Enomoto, S. Jogan, and T. Hashimoto, *Metal. Mater. Trans. A*, **30**, 3125 (1999).
15. W. B. Lee, Y. M. Yeon, and S. B. Jung, *Mater. Sci. Technol.*, **19**, 1513 (2003).
16. C. Gallais, A. Simar, D. Fabregue, A. Denquin, G. Lapasset, B. de Meester, Y. Brechet, and T. Pardoen, *Metal. Mater. Trans. A*, **38**, 964 (2007).
17. R. S. Mishra and Z. Y. Ma, *Mater. Sci. Eng. R*, **50**, 1 (2005).
18. J. Q. Su, T. W. Nelson, and C. J. Sterling, *Scri. Mater.*, **52**, 135 (2005).
19. P. B. Prangnell and C. P. Heason, *Acta Mater.*, **53**, 3179 (2005).
20. W. Woo, H. Choo, D. W. Brown, P. K. Liaw, and Z. Feng, *Scri. Mater.*, **54**, 1859 (2006).
21. Z. Y. Ma, R. S. Mishra, and M. W. Mahoney, *Acta Mater.*, **50**, 4419 (2002).
22. Z. Y. Ma and R. S. Mishra, *Acta Mater.*, **51**, 3551 (2003).
23. C. J. Hsu, C. Y. Chang, P. W. Kao, N. J. Ho, and C. P. Chang, *Acta Mater.*, **54**, 5241 (2006).
24. L. B. Johannes and R. S. Mishra, *Mater. Sci. Eng. A*, **464**, 255 (2007).
25. Z. Y. Ma, S. R. Sharma, and R. S. Mishra, *Scri. Mater.*, **54**, 1623 (2006).
26. Z. Y. Ma, S. R. Sharma, and R. S. Mishra, *Scri. Mater.*, **54**, 1623 (2006).
27. M. M. El-Rayes and E. A. El-Danaf, *J. Mater. Process. Technol.*, **212**, 1157 (2012).
28. K. J. Al-Fadhalah, A. I. Almazrouee, and A. S. *Mater. Des.*, **53**, 550 (2014).
29. F. Gharavi, K. A. Matori, R. Yunus, and N. K. Othman, *Mat. Res.*, **17**, 1563 (2014).
30. V. Fahimpour, S. K. Sadrnezhaad, and F. Karimzadeh, *Mater. Des.*, **39**, 329 (2012).
31. F. Gharavi, K. A. Matori, R. Yunus, N. K. Othman, and F. Fadaeifard, *J. Mater. Res. Technol.*, **4**, 314 (2015).
32. M. Esmaily, M. Shahabi-Navid, J. E. Svensson, M. Halvarsson, L. Nyborg, and Y. Cao amd L. G. Johansson, *Corros. Sci.*, **90**, 420 (2015).
33. M. Esmaily, N. Mortazavi, M. Shahabi-Navid, J. E. Svensson, M. Halvarsson, L. Nyborg, A. E. W. Jarfors, M. Wessén, and L. G. Johansson, *J. Electrochem. Soc.*, **162**, C85 (2015).
34. M. Esmaily, M. Shahabi-Navid, N. Mortazavi, J. E. Svensson, M. Halvarsson, Y. Cao, and L. G. Johansson, *J. Electrochem. Soc.*, **162**, C311 (2015).
35. M. Shahabi-Navid, M. Esmaily, J. E. Svensson, M. Halvarsson, L. Nyborg, Y. Cao, and L. G. Johansson, *J. Electrochem. Soc.*, **161**, C277 (2014).
36. B. Li, Y. Shen, and W. Hu, *Mater. Des.*, **32**, 2073 (2011).
37. Y. S. Sato, H. Takauchi, S. Hwan, C. Park, and H. Kokawa, *Mater. Sci. Eng. A.*, **405**, 333 (2005).
38. T. Watanabe, *Res. Mech.*, **11**, 47 (1984).
39. N. Birbilis, *Corrosion*, In-Press, (2015), DOI: 10.5006/1703.
40. N. Birbilis, R. Zhang, M. L. C. Lim, R. K. Gupta, C. H. J. Davies, S. P. Lynch, R. G. Kelly, and J. R. Scully, *Corrosion*, **69**, 396 (2013).
41. R. K. Gupta, R. Zhang, C. H. J. Davies, and N. Birbilis, *Corrosion*, **70**, 402 (2014).
42. R. K. Gupta, Y. Wang, R. Zhang, N. L. Sukiman, C. H. J. Davies, and N. Birbilis, *Corrosion*, **69**, 4 (2013).
43. M. H. Larsen, J. C. Walmsley, O. Lunder, R. H. Mathiesen, and K. Nisancioglu, *J. Electrochem. Soc.*, **155**, C550 (2008).
44. W. J. Poole, M. A. Wells, and D. J. Lloyd, *Mater. Sci. Forum*, **519–521**, 1721 (2006).
45. P. J. Gregson and S. Harris, *Mater. Sci. Forum*, **396–402**, 601 (2002).
46. S. Foss, A. Olsen, C. J. Simensen, and J. Tafto, *Acta Crystal.*, **B59**, 36 (2003).
47. G. S. Frankel, *J. Electrochem. Soc.*, **145**, 2186 (1998).
48. N. Birbilis and R. G. Buchheit, *J. Electrochem. Soc.*, **152**, B140 (2005).
49. N. Birbilis, M. K. Cavanaugh, and R. G. Buchheit, *Corros. Sci.*, **48**, 4202 (2006).
50. N. Birbilis and R. G. Buchheit, *J. Electrochem. Soc.*, **155**, C117 (2008).
51. T. Dorin, N. Stanford, N. Birbilis, and R. K. Gupta, *Corros. Sci.* **100**, 396 (2015).
52. J. O. Park, C. H. Paik, Y. H. Huang, and R. C. Alkire, *J. Electrochem. Soc.*, **146**, 517 (1999).
53. R. Nandan, G. G. Roy, T. J. Lienert, and T. DebRoy, *Sci. Technol. Weld. Join.*, **11**, 526 (2006).
54. J. H. Cho, D. E. Boyce, and P. R. Dawson, *Mater. Sci. Eng. A*, **398**, 146 (2005).